

Chiral and SHG-Active Metal–Organic Frameworks Formed in Solution and on Surfaces: Uniformity, Morphology Control, Oriented Growth, and Postassembly Functionalization

Qiang Wen, Shira Tenenholtz, Linda J. W. Shimon, Omri Bar-Elli, Lior M. Beck, Lothar Houben, Sidney R. Cohen, Yishay Feldman, Dan Oron, Michal Lahav,* and Milko E. van der Boom*



Cite This: *J. Am. Chem. Soc.* 2020, 142, 14210–14221



Read Online

ACCESS |



Metrics & More

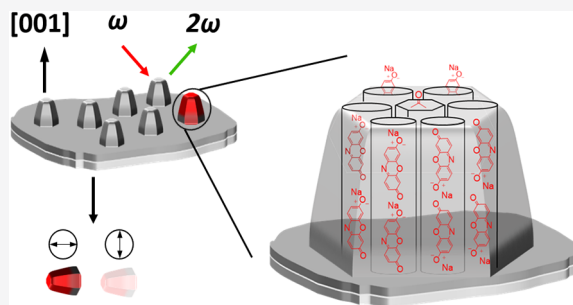


Article Recommendations



Supporting Information

ABSTRACT: We demonstrate the formation of uniform and oriented metal–organic frameworks using a combination of anion effects and surface chemistry. Subtle but significant morphological changes result from the nature of the coordinative counteranion of the following metal salts: NiX_2 with $\text{X} = \text{Br}^-$, Cl^- , NO_3^- , and OAc^- . Crystals could be obtained in solution or by template surface growth. The latter results in truncated crystals that resemble a half structure of the solution-grown ones. The oriented surface-bound metal–organic frameworks (sMOFs) are obtained via a one-step solvothermal approach rather than in a layer-by-layer approach. The MOFs are grown on Si/SiOx substrates modified with an organic monolayer or on glass substrates covered with a transparent conductive oxide (TCO). Regardless of the different morphologies, the crystallographic packing is nearly identical and is not affected by the type of anion or by solution versus the surface chemistry. A propeller-type arrangement of the nonchiral ligands around the metal center affords a chiral structure with two geometrically different helical channels in a 2:1 ratio with the same handedness. To demonstrate the accessibility and porosity of the macroscopically oriented channels, a chromophore (resorufin sodium salt) was successfully embedded into the channels of the crystals by diffusion from solution, resulting in fluorescent crystals. These “colored” crystals displayed polarized emission (red) with a high polarization ratio because of the alignment of these dyes imposed by the crystallographic structure. A second-harmonic generation (SHG) study revealed Kleinman symmetry-forbidden nonlinear optical properties. These surface-bound and oriented SHG-active MOFs have the potential for use as single nonlinear optical (NLO) devices.



INTRODUCTION

The morphology and uniformity of crystals are fascinating structural properties that are difficult to predict and design.^{1–3} The relationship between the structure of the molecular components and their crystal appearance (e.g., unit cell structure and macroscopic crystalline shape) is often not obvious.^{4,5} Crystal design often includes the use of additives or modulators. For example, Wang, Sun, and Yaghi demonstrated that the use of nucleation inhibitors resulted in the formation of covalent organic frameworks suitable for single-crystal X-ray diffraction.⁶ Surface chemistry has also been used to direct and control the crystallization of diverse materials on inorganic surfaces, (patterned) monolayers, and others as shown by Aizenberg and Whitesides.^{7,8} Interface chemistry played a pivotal role in fundamental studies in crystal nucleation by Leiserowitz, Lahav, Weissbuch, and Sagiv using Langmuir–Blodgett films of amino acids.⁹ These and other approaches have been shown to be powerful tools to control growth and even chirality.¹⁰ Bottom-up approaches, based on the structure and properties of the components, are often utilized to control the molecular packing,¹¹ photo-

chemical reactivity,^{12,13} and porosity.¹⁴ To date, no generally applicable approach exists, and there is insufficient fundamental understanding of the pathway to bottom-up formation of uniform crystals having defined sizes and shapes.^{2,3,15,16}

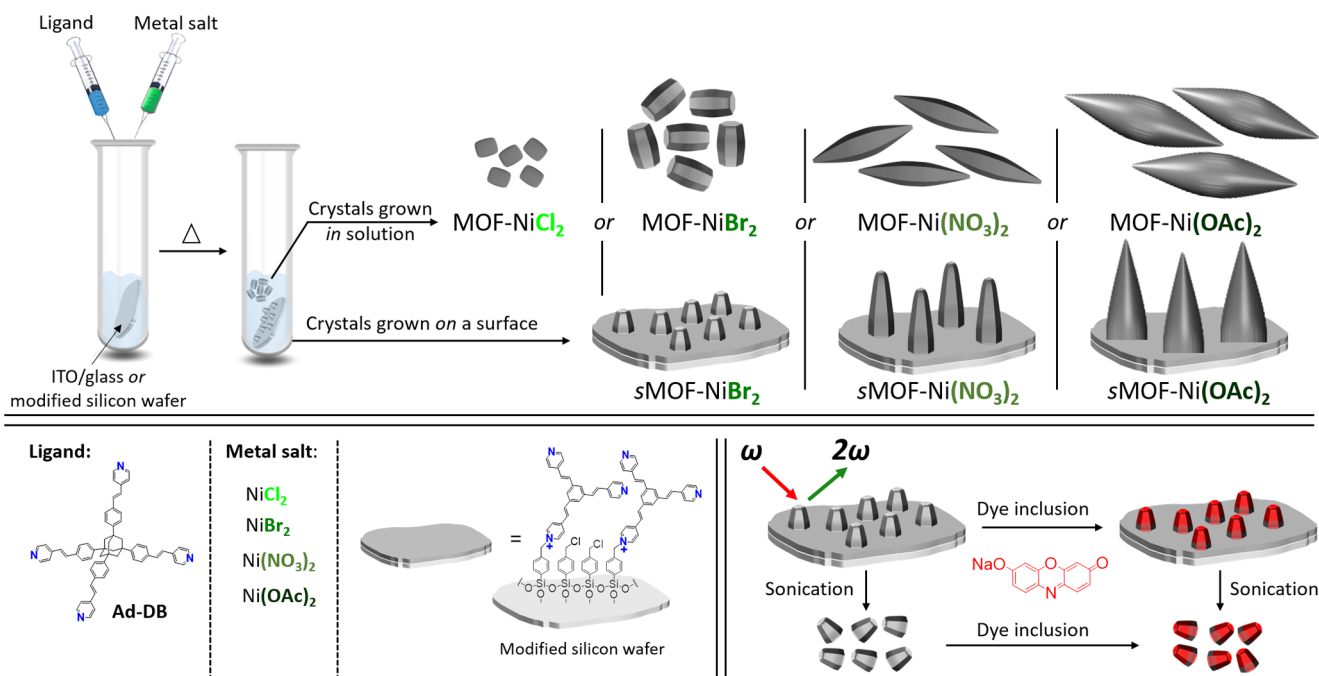
Modulators and additives have also been used to control uniformity of metal–organic frameworks (MOFs).^{16–18} For example, lauric acid or *n*-dodecanoic acid has been used to control the morphology of $[\text{Cu}_3(\text{btc})_2]_n$ (btc = benzene-1,3,5-tricarboxylate).¹⁸ Designing both molecular-level organization and crystal morphology still remains a challenge. MOFs represent an important class of crystalline materials with many potential applications.^{19–21} Their tunable and permanent porosity, huge surface area, and stability make them ideal

Received: May 16, 2020

Published: July 10, 2020



Scheme 1. (Top) Concurrent Formation of Uniform Metallo-organic Crystals in Solution and on Surfaces (sMOFs) under Solvothermal Conditions;^a (Bottom) Inclusion of Dyes and Surface Detachment of NLO-Active Crystals by Sonication^{b,c}



^aThe crystal morphology and dimensions can be modified by varying the counteranions of the nickel salts. Ad-DB = 1,3,5,7-tetrakis(4-((E)-2-(pyridin-4-yl)vinyl)-phenyl)adamantane. ^bAnions (Cl⁻) of the monolayer are not shown. ^cPostassembly functionalization by inclusion and alignment of dye molecules (sodium resorufin) in helical channels perpendicular to the substrate surface.

candidates for energy storage,^{22–27} separation,^{24,28–31} chemical sensing,³² and catalysis.^{33–35} Chiral chemistry with MOFs is also of much interest.³⁶ For example, enantioselective catalysis,³⁷ chiral sensing³⁸ and separation³⁹ have been demonstrated with such materials. The design principles of MOFs, like any crystal, are highly complex and include many parameters and requirements.⁴⁰ For example, (I) the counteranions of metal salts, which are used in the synthesis of MOFs, play an important role in their growth. Negatively charged carboxylate-based ligands at least partially balance the positive charges of the metal centers.⁴¹ The use of neutral pyridine-based ligands requires counteranions to compensate for the positive charge of frameworks. A clear correlation between the nature of the applied counteranions, the formed crystals, and their growth mechanism is not obvious.⁴² Another example (II) is the surface-induced structural features versus growth in solution. Interpenetration of molecular networks, and hence the porosity, can be drastically affected by growing MOFs on surfaces. Surface-mounted MOFs (SURMOFs) were introduced by Wöll and Fisher.^{43,44} The preparation of these thin films involves dip and spray coating techniques.^{43,45} Applications of these monolithic and homogeneous coatings include sensing, gas separation, and membrane technology.^{29,46–54} (III) The orientation of crystals on surfaces is also an important structural feature (e.g., for the formation of organic resonators⁵⁵ and efficient use of channels^{56–58}). Methods to achieve macroscopically oriented MOFs are mainly related to carboxylate-ligand chemistry and specific structures. Oriented pyridine-ligand-based MOFs have been less studied, although pyridine is known to be a useful ligand in the rich chemistry of transition metal complexes. Stang,⁵⁹ Futija,⁶⁰ and others^{61–64} introduced many architectures with well-defined geometries and shapes.

We have previously shown that the coordination chemistry of tetrahedral pyridine-based ligands offers opportunities to synthesize diverse structures, each expressing high uniformity.⁶⁵ On the basis of copper and nickel salts, they assume various forms including rare single crystals having a multi-domain “yo-yo-like” appearance.⁶⁶ These unique enantiopure crystals are formed from achiral components, and their growth progresses with striking morphological changes. We have also demonstrated the metal-mediated formation of fused and hollow organic crystals.⁶⁷ Furthermore, these pyridine-based ligands have been used for the formation of three-dimensional halogen-bond-based organic frameworks (XBOFs).⁶⁸

We demonstrate here the macroscopically oriented growth of metallo-organic crystals with control over the crystal morphology and dimensions (Scheme 1). Our crystals exhibit a high level of uniformity in shape and size without the use of additives or modulators. The crystallographic structures have a unique molecular arrangement: The dense and chiral packing of achiral building blocks with the rare space group *P622* form single crystals expressing both enantiomorphs. The crystals are formed under solvothermal reaction conditions. Their macroscopic structures were systematically changed by (i) solution versus surface chemistry, (ii) varying the anion, and (iii) changing the concentration of both the metal salt precursor and the organic ligand. The molecular packing is practically invariant for these different crystallization conditions. The surface-bound crystals are truncated and resemble one-half of the morphology of those grown in solution and can be detached by sonication. These crystals, grown on an organic monolayer on silicon and quartz substrates or directly on bare indium–tin-oxide substrates, are orientated with their continuous channels perpendicular to the substrate surface. These well-defined channels are chemically accessible for the

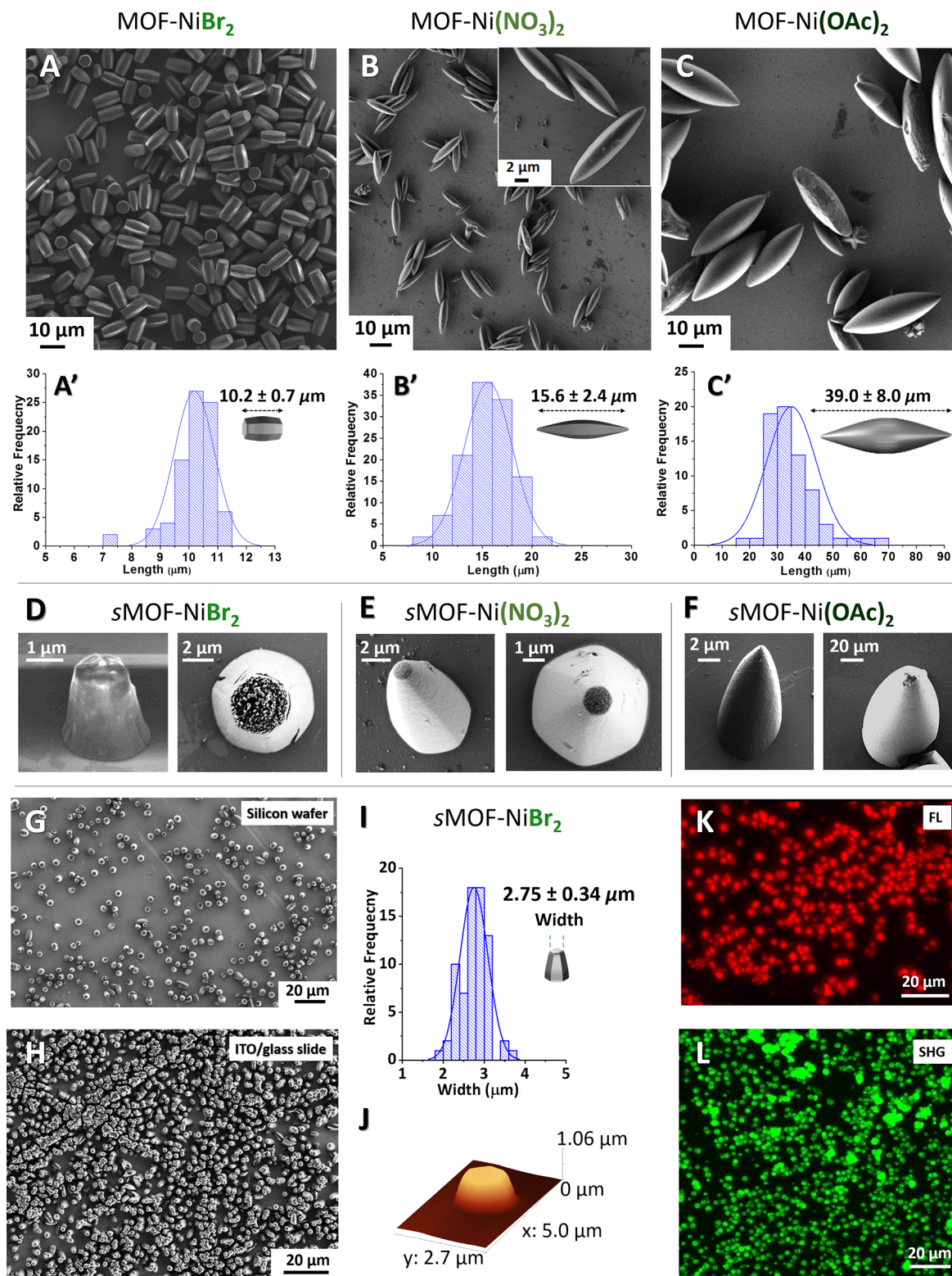


Figure 1. Morphological analysis of the metal-organic crystals formed in solution and on the surface (sMOFs). (A–C) Scanning electron microscope (SEM) images of MOF-NiBr_2 (hexagonal prism), $\text{MOF-Ni(NO}_3)_2$ (oval), MOF-Ni(OAc)_2 (oval), and (A'–C') corresponding histograms showing the length distribution. (D–F) SEM images of sMOF-NiBr_2 , $\text{sMOF-Ni(NO}_3)_2$, and sMOF-Ni(OAc)_2 on a silicon wafer coated with a covalently bound organic monolayer. (G) Zoom-out SEM image of sMOF-NiBr_2 shown in D. (H) SEM image of sMOF-NiBr_2 on ITO/glass. (I) Histogram showing the width distribution of the hexagonal face of data shown in G. (I) AFM image of sMOF-NiBr_2 on a silicon wafer coated with a covalently bound organic monolayer (Scheme 1). (J) Confocal fluorescent images of sMOF-NiBr_2 on ITO/glass after inclusion of sodium resorufin, $\lambda_{\text{exc}} = 561 \text{ nm}$, $\lambda_{\text{em}} = 571\text{--}649 \text{ nm}$. (K) Second-harmonic generation (SHG) microscope image of sMOF-NiBr_2 on ITO/glass, $\lambda_{\text{in}} = 940 \text{ nm}$, $\lambda_{\text{out}} = 470 \text{ nm}$.

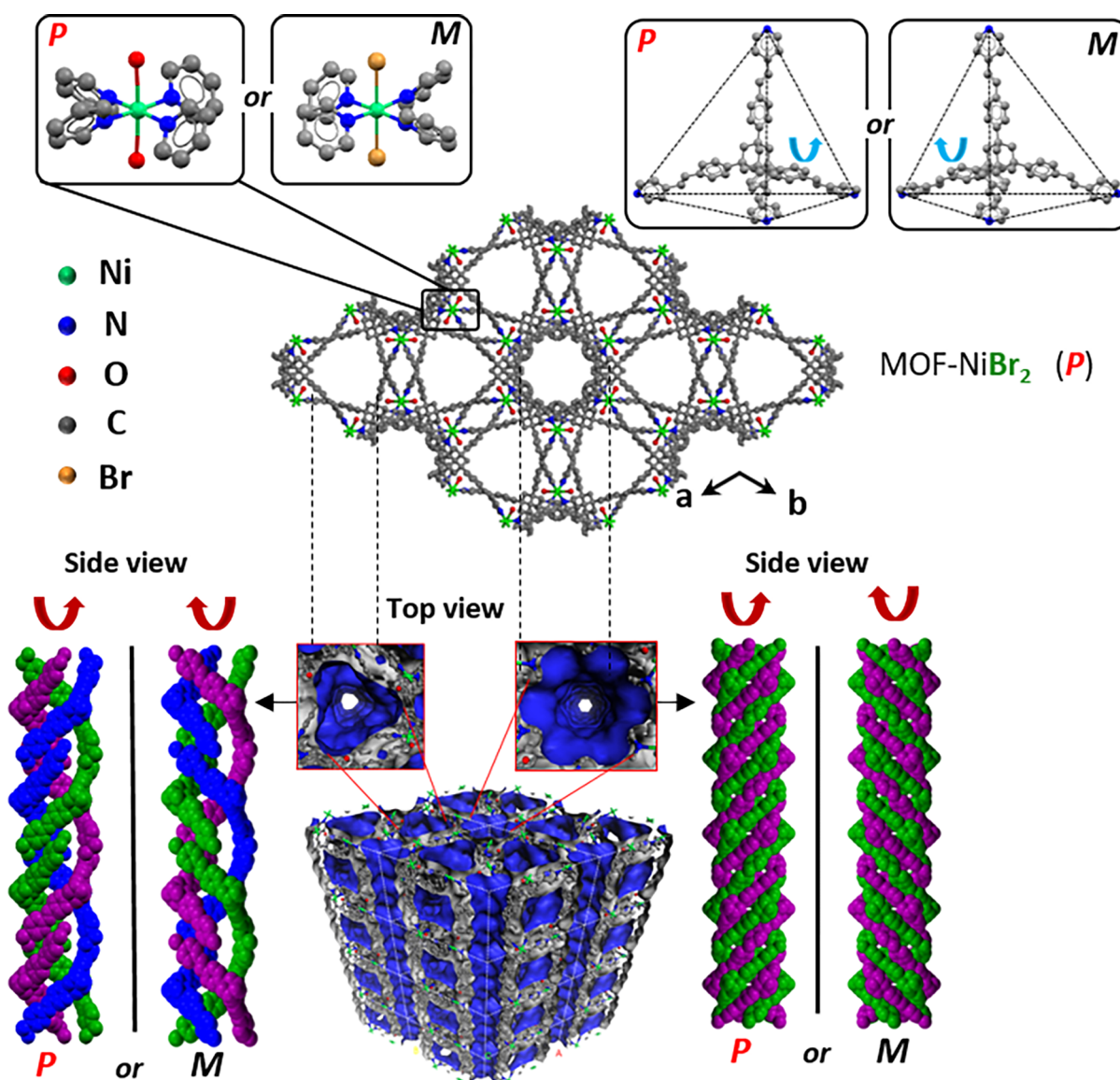


Figure 2. Two X-ray crystal structures of enantiomorphs of MOF-NiBr₂: ball and stick representation of the framework viewed from the *c* axis. (Top left) Octahedral coordination of the metal center. Pyridine moieties forming a propeller-type arrangement. (Top right) Distorted structure of Ad-DB. Perspective and side view of two different helical channels with the Connolly surface shown in blue. Hydrogen atoms have been omitted for clarity. *P* = CCDC1965786, *M* = CCDC1965784 (Table S1). The axial ligands coordinating to the metal center are from H₂O (MOF-NiBr₂-*P*) or Br⁻ (MOF-NiBr₂-*M*).

supramolecular organization of guest molecules. Both the solution- and the surface-bound crystals showed strong Kleinman symmetry-forbidden second-order nonlinear properties.⁶⁹

RESULTS AND DISCUSSION

Reaction of the ligand 1,3,5,7-tetrakis(4-((*E*)-2-(pyridin-4-yl)vinyl)phenyl)adamantane (Ad-DB) with NiX₂ (X = Cl⁻, Br⁻, NO₃⁻, or CH₃COO⁻) was carried out in a molar ratio of 1:2 under solvothermal conditions at 105 °C. This reaction mixture was heated in dimethylformamide (DMF) and chloroform (9:1 v/v) for 48 h in a sealed glass pressure vessel and gradually cooled down to room temperature. A light green powder was isolated by centrifugation and subsequently washed with common organic solvents (Scheme 1). Scanning electron microscope analysis revealed microstructures having a high level of uniformity, both in size and in

morphology (Figures 1A–C and S1). Two distinct morphologies were observed: (i) hexagonal-like rods for X = Cl⁻ or Br⁻ and (ii) oval-shaped morphologies for X = NO₃⁻ or CH₃COO⁻. Despite the morphological similarities and high level of uniformity, the average sizes of the different crystals vary significantly. This difference between the average length of the crystals formed from NiCl₂ versus NiBr₂ is large (0.5 ± 0.1 μm versus 10.2 ± 0.7 μm, respectively). The small size of the crystals formed with NiCl₂ is in the range of colloidal-sized objects. The difference (2.5×) in the length of the oval-shaped crystals formed from Ni(NO₃)₂ versus Ni(OAc)₂ (15.6 ± 2.4 or 39.0 ± 8.0 μm, respectively) also demonstrates that the nature of the anion largely determines both the dimensions and the morphology. These observations indicate that the nucleation process with NiCl₂ is relatively fast; formation of larger numbers of seeds is expected to result in smaller sized crystals. Varying the concentrations of Ad-DB

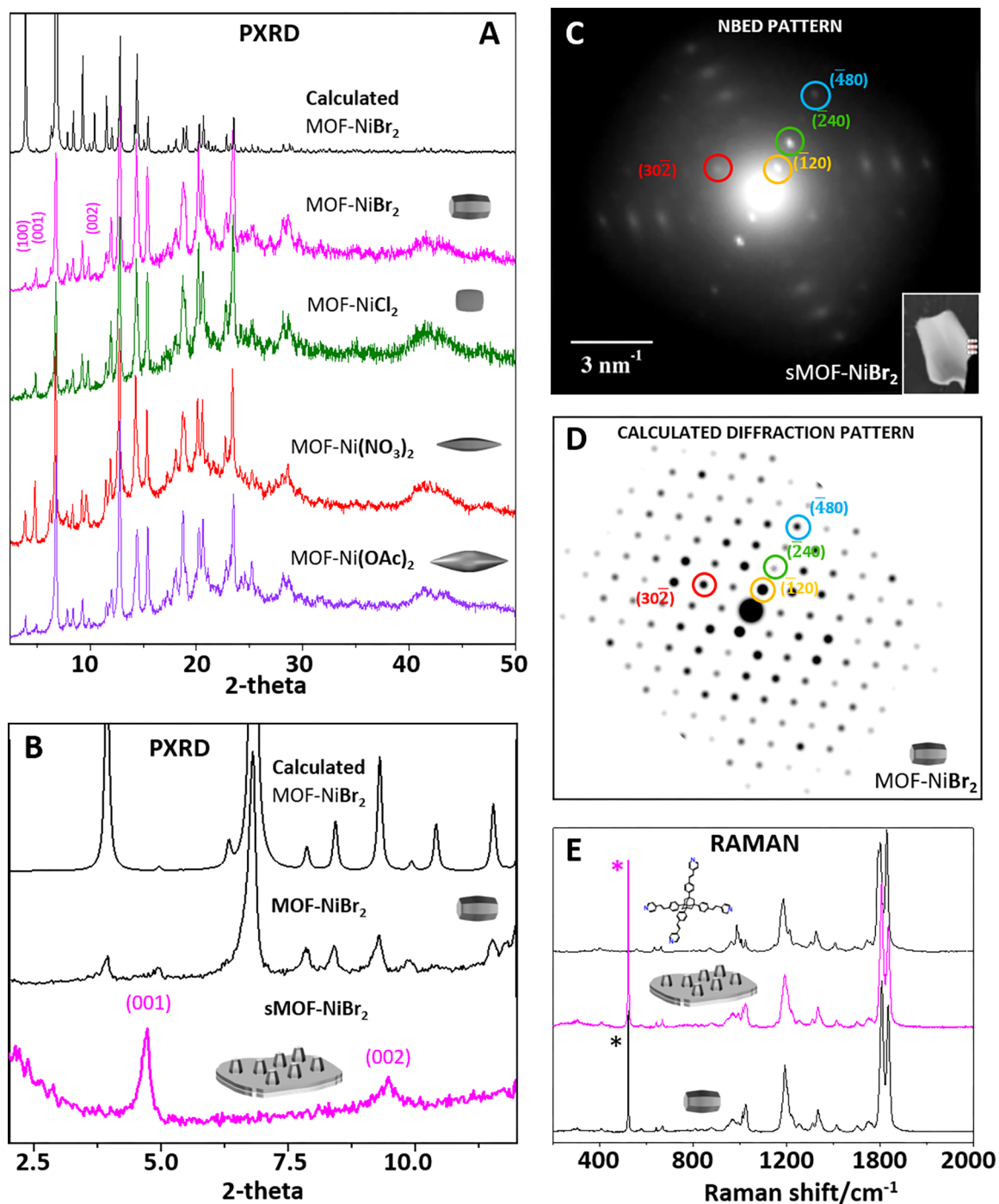


Figure 3. Structural characterization of solution-grown and surface-bound MOFs (sMOFs). (A) Powder X-ray diffraction (PXRD). Single-crystal data of MOF-NiBr_2 was used to obtain the calculated pattern (black). (B) PXRD of sMOF-NiBr_2 on ITO/glass, the calculated diffraction pattern, and experimental diffraction pattern of MOF-NiBr_2 . (C) Experimental nanobeam electron diffraction (NBED) pattern of sMOF-NiBr_2 detached by sonication. Circles in C and D denote matching diffractions. (D) Simulated selected area electron diffraction from the single-crystal data of MOF-NiBr_2 . (E) Micro-Raman spectra on silicon substrates, from top to bottom: Ad-DB, sMOF-NiBr_2 on a silicon wafer coated with a covalently bound organic monolayer (Scheme 1), and MOF-NiBr_2 . Asterisk denotes (*) silicon background: $\lambda = 520 \text{ cm}^{-1}$.

and NiBr_2 while keeping their molar ratios constant at 1:2 revealed a nonlinear relationship between the concentration and the crystal dimensions (Figure S2). Increasing the concentrations reduced the crystal length from $\sim 35 \mu\text{m}$ at low concentration to $\sim 2.5 \mu\text{m}$ at the highest concentration used. In addition, in this experiment the crystals all displayed a similar morphology despite the large size range and uniform size for each concentration. These observations are consistent

with the LaMer model for crystal growth: low concentrations induce a slow nucleation, affording large crystals, whereas high concentrations result in fast nucleation, resulting in small crystals.

Four single-crystal X-ray diffraction analyses were performed on two sets of morphologically different crystals. These crystals were obtained using NiBr_2 and Ni(OAc)_2 (Figures 1 and 2 and Table S1). The X-ray diffraction pattern

is well ordered, and the reflections are well defined and separated, indicative of single crystals. Their crystallinity is also apparent from the birefringence observed with Cross-Nicols polarized microscopy (Figures S3–S6). The materials crystallized in a rare, hexagonal space group ($P622$) with the crystallographic C_3 and C_6 axes passing through helical channels. The Flack parameters of the two crystals obtained from NiBr_2 are 0.059(13) and 0.027(16). For the oval-shaped MOFs prepared with $\text{Ni}(\text{OAc})_2$, the Flack parameters are 0.06(5) and 0.06(6). These four near-zero values indicate that the absolute structure determined by our structure refinement is correct and that these crystals are not twinned.⁷⁰ For each set of two crystals, we observed crystals having a packing with opposite handedness. Thus, the individual crystals are enantiomerically pure, and the batches of crystals consist of mixtures of enantiomorphs.

The coordination geometry around the nickel center is twisted octahedral for all four structures with two oxygens or counteranions in the axial position and four pyridine nitrogen donors in the equatorial plane. The coordination geometry and bond distances are in agreement with the d^8 nickel–pyridine complexes.⁷¹ For example, for crystals formed from **Ad-DB** and NiBr_2 , the bond distances are $\text{Ni–N} = 2.050 \text{ \AA}$ and $\text{Ni–O} = 2.470 \text{ \AA}$ (CCDC 1965786). The axial oxygens coordinating to the metal center are from H_2O . The anions of $\text{MOF–Ni}(\text{OAc})_2$ are not part of the crystallographic structure; however, their presence has been indicated by infrared spectroscopy at $\nu = 1653 \text{ cm}^{-1}$. The anions of $\text{MOF–Ni}(\text{NO}_3)_2$ were observed at $\nu = 1384$ and 1627 cm^{-1} (Figures S7 and S8). We previously reported the formation of paradoxical multidomain single crystals formed from a similar ligand (having triple instead of double carbon–carbon bonds) and $\text{Cu}(\text{NO}_3)_2$.⁶⁶ Although morphologically completely different, these crystals have a molecular packing nearly identical to the crystals reported here. These observations show that varying the anion (Br^- , Cl^- , NO_3^- , and OAc^-) and metal cation (Cu vs Ni) in the presence of these ligands results in varied morphologies (shape, mono- to multidomain) and dimensions while retaining a high level of uniformity and nearly identical crystallographic structures. Two structural features are apparent, namely, chirality and topology. The origin of the chirality and handedness is probably related to the coordination of the pyridine moieties of the ligands to the metal centers. The pyridine moieties are arranged in a four-blade propeller-type fashion around the metal center to minimize the steric hindrance. Such conformation is known for bivalent nickel complexes having four pyridine ligands.^{72–75} However, the crystal structures of such nickel complexes mainly consist of a racemic mixture. For example, the unit cell of dichlorotetrakis(pyridine)nickel(II) contains four pairs of complexes having an opposite “propellers” arrangement.⁷⁵ The unit cells of our MOFs contain only propellers having the same handedness, hence the symmetry breaking. Crystals having the same handedness have the same propeller-type conformations (Figure 2). Interestingly, the achiral **Ad-DB** is arranged as a chiral, slightly distorted tetrahedral structure. In contrast, the crystal structure of the ligand alone shows an achiral molecular arrangement (Figure S9). A similar effect has also been observed for SiO_4 in quartz and some chiral zeolites.⁷⁶ Topological analysis revealed a quadrupally connected tetrahedral ligand bridged by the metal center, resulting in a unique binodal net (Figure S10) not found in the database of ToposPro (which is based on the

data of the Cambridge Crystallographic Data Centre).⁷⁷ The Connolly surface shows two types of channels along the c axis. Space-filling representations and the simplified network clearly show the presence of two kinds of channels having diameters of ~ 7.0 and $\sim 10.2 \text{ \AA}$. The hexagonal channel is formed by six helical chains running around the C_6 symmetry axis. The triangular channel is generated by three helical chains related by a C_3 symmetry axis. The chirality is expressed at three levels: the metal–ligand coordination, the distortion of the ligand, and the helical chains (Figure 2).

Powder X-ray diffraction (PXRD) analysis revealed that the four morphologically different crystals have a very similar molecular packing regardless of the nickel salt used (Figure 3A). Differences in the relative intensity of some peaks, e.g., (100) and (001), may be caused by morphological differences due to the presence of the different anions. The phase purity of the bulk samples is confirmed by comparing the observed powder X-ray diffraction (PXRD) patterns with the calculated patterns. These calculated patterns were obtained from the single-crystal X-ray analysis of crystals formed from **Ad-DB** and NiBr_2 (vide infra).

We succeeded to grow orientated MOFs from **Ad-DB** and NiX_2 (Br^- , NO_3^- , and OAc^-) on various substrates that were placed in solutions in the glass pressure vessels (Scheme 1).⁷⁸ Silicon and quartz substrates were first coated with a monolayer to generate a pyridine-terminated surface that would allow the nickel salts to bind. Similar results were obtained with the same monolayers bound to quartz. No crystal growth was observed on bare silicon and quartz substrates. SEM images of silicon substrates functionalized with the organic monolayer show structures having a high level of uniformity and directionality (Scheme 1, Figure 1D–G). The anion-morphology relationship observed for the solution-grown crystals is also clear for the on-surface MOFs. In all cases, the shapes of the surface-bound crystals reflect truncated morphologies with approximately one-half the structure of the crystals that were grown concurrently in solution. In addition to the different shapes, the on-surface crystals are smaller in comparison with the crystals formed in solution. Compared to homogeneous crystallization, the relatively low nucleation energy barrier for on-surface crystallization can result in the rapid formation of numerous nuclei. Such a process would be accompanied by the consumption of the starting materials at the surface–solution interface, resulting in smaller crystals. Strain can also determine crystal sizes at surfaces. Statistical analysis of the SEM data (100 crystals) revealed that the width of the hexagonal face is $2.75 (\pm 0.34) \mu\text{m}$ (Figure 1I). Measurements by AFM show the surface-bound crystals of **Ad-DB** and NiBr_2 are $\sim 1 \mu\text{m}$ in height and width (Figures 1J and S11, S12). The elastic modulus of these crystals is $7.3 \pm 2 \text{ GPa}$, which is comparable to the reported values of organic crystals and MOFs.^{65,79}

Interestingly, using bare indium–tin oxide (ITO)-coated glass substrates for the formation of surface-bound MOFs from NiBr_2 , we succeeded to increase their density, further reducing their size ($\sim 2\times$) while maintaining the same morphology (Figure 1H). Metal–oxide surfaces can bind metal salts. The relatively high roughness of ITO is a factor that might enhance the formation of more nuclei, resulting in smaller crystals ($\sim 1.0 \mu\text{m}$ width).

The dimensions of the surface-bound MOFs can also be controlled as a function of the concentration of both the metal

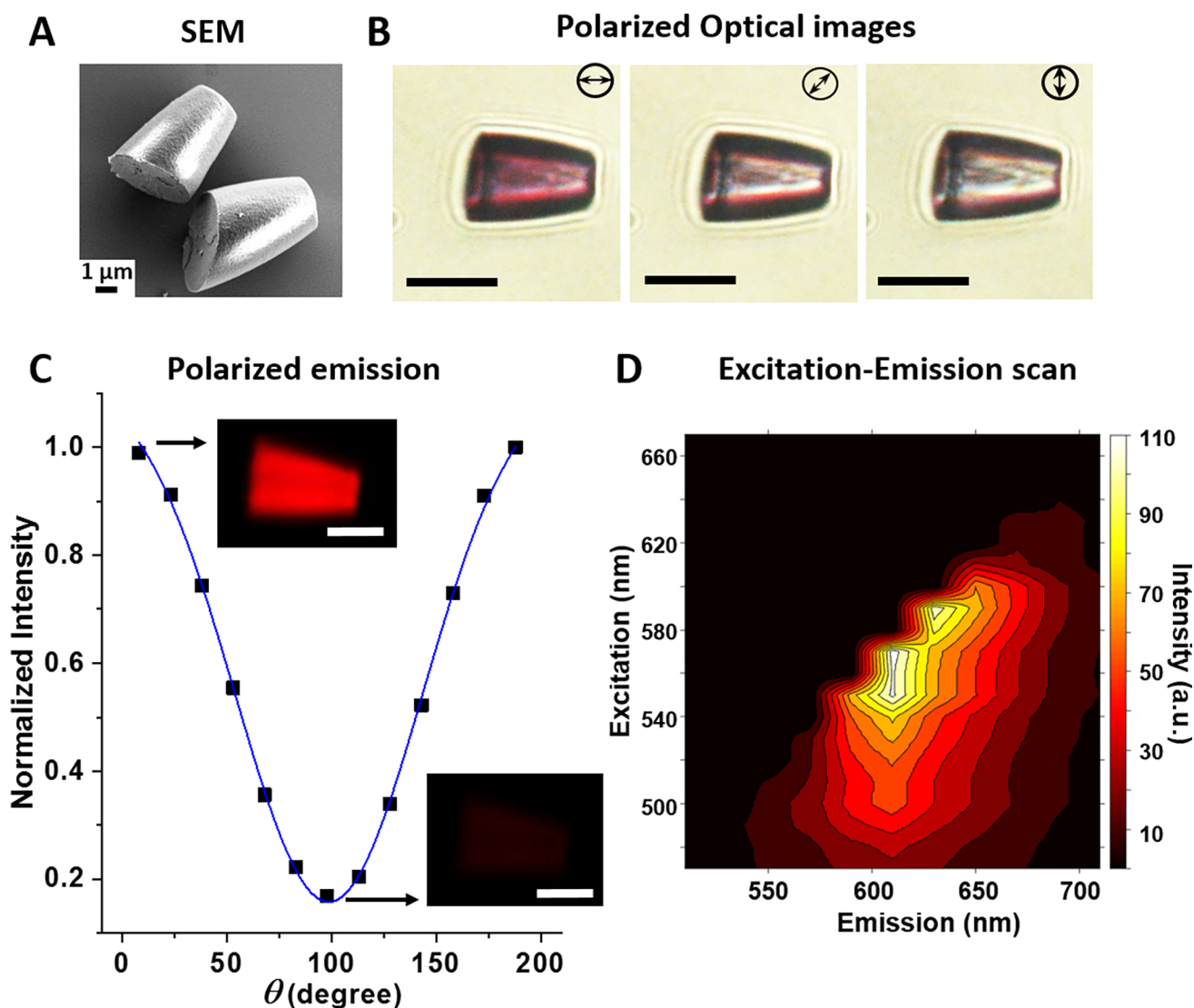


Figure 4. sMOF-NiBr₂ after surface detachment and functionalization with sodium resorufin. (A) SEM image prior to chromophore inclusion. (B) Optical images of dye-loaded crystals under polarized light. Scale bar: 10 μ m (C) Polarized-dependent emission. (Inset) Fluorescent images, $\lambda_{\text{exc}} = 561$ nm, collected at $\lambda = 571\text{--}649$ nm. Scale bar: 5 μ m. θ is defined as the polarization direction of the laser beam related to the c axis of the crystal. (D) Excitation–emission spectrum showing two main emission peaks at $\lambda = 610$ and 635 nm.

salt precursor and Ad-DB, similar to our observations for crystal growth in solution (Figure S2). We demonstrated this effect by reducing the concentrations by a factor of 3 for both NiBr₂ and Ad-DB while keeping all other reaction parameters identical. By doing so, the width of the surface-bound crystals increased by a factor of 5, from ~ 2.8 to ~ 14.0 μ m. Concurrently, the area density of the surface-bound crystals dropped significantly. For example, only a few crystals are found in an area of 170 μ m \times 150 μ m (Figure S13) because of the lower concentration of nuclei. Neither the uniformity nor the morphology was affected.

The above-discussed observations might suggest that crystal growth in solution and on the surface proceeds via the same mechanistic pathway. One difference that we observed is the secondary growth of morphologically identical small crystals on the surface of some of the surface-bound crystals (Figure S14). These nanosized crystals are as small as ~ 34 nm. The formation of these structures might indicate that the initial surface-bound crystals are formed on reactive, defect areas. In time, these reactive areas become covered, whereas the surface

areas of the surface-bound crystals increased and became competitive as templates for crystallization.

A focused ion beam (FIB) microscope was used to cross-section both the solution and the on-surface crystals generated from NiBr₂. Analysis of the on-surface-bound crystals showed defects, especially found at the side bound to the substrate surface. However, no such cracks were found in smaller sized crystals. Consistently, solid and intact inner structures for the solution-grown crystals were observed (Figure S15). These observations suggest that the combination of relatively rapid growth as well as defects at the substrate interface can cause these structural flaws. Nevertheless, the crystal morphology is not affected. The crystallinity of the surface-bound MOFs grown from AD-DB and NiBr₂ was demonstrated by (i) PXRD (Figure 3B), (ii) the birefringence observed in the Crossed-Nicols polarized micrographs (Figure S16), and (iii) electron diffraction (Figure 3C).

PXRD indicated the crystallinity and the orientation of these sMOFs. These measurements showed two sharp diffraction peaks (4.73 and 9.47 at 2θ), which we assigned

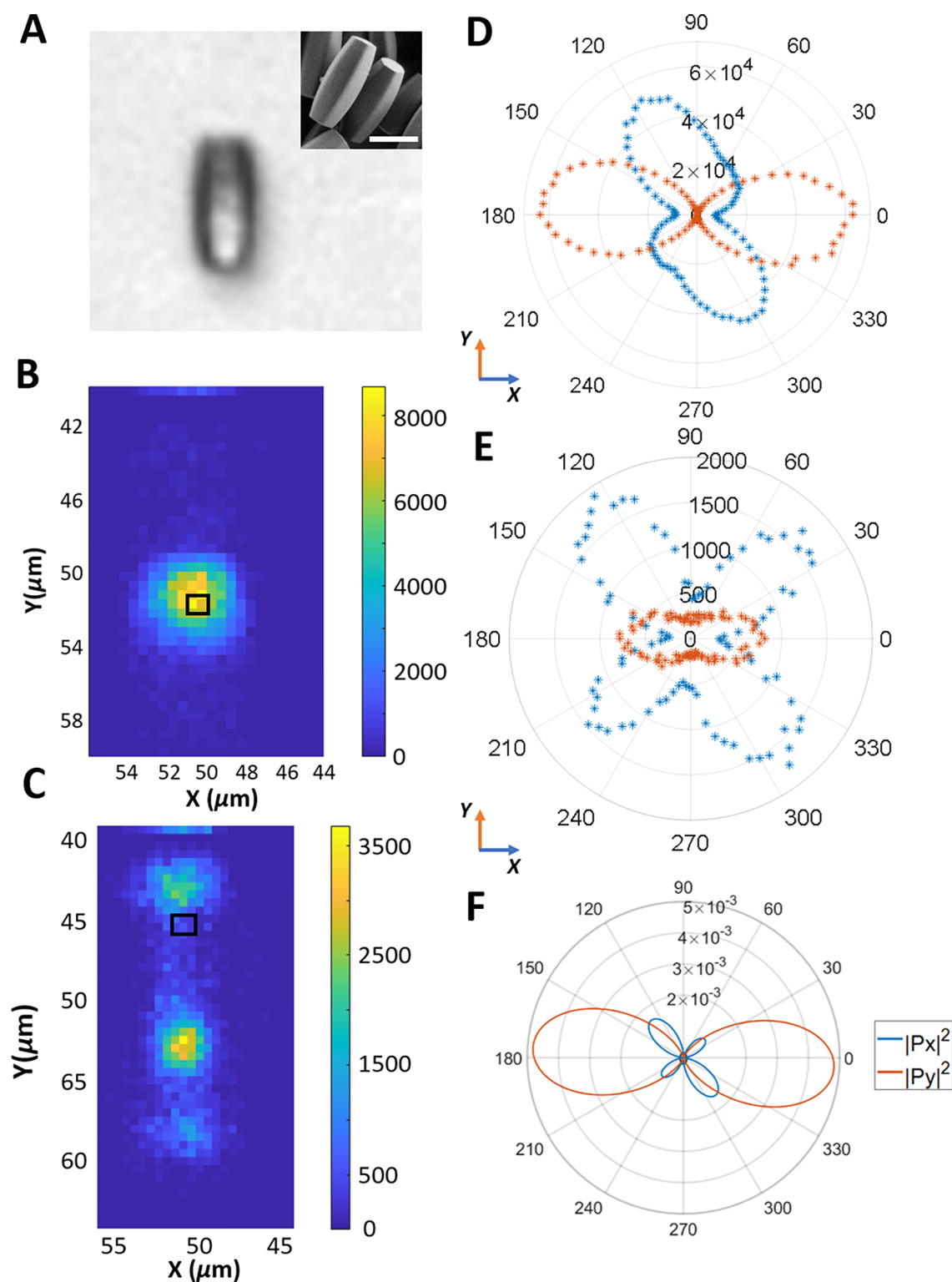


Figure 5. Raster scans and polarization-dependent measurements of a single crystal of MOF-NiBr₂, with different excitation and collection polarizations ($\lambda_{\text{ex}} = 1000$ nm). (A) Optical image of the measured crystal. (Inset) SEM image; scale bar 10 μm . (B) Lab x -axis direction. (C) Lab y -axis direction. (D) Polar plot of the SHG intensity at the location indicated in B. (E) Polar plot of the SHG intensity at the location indicated in C. For D and E, the blue and red plots are the x - and y -polarization components, respectively, collected through a polarizer. (F) Simulated SHG based on the 622 symmetry.

as (001) and (002). This assignment is based on a comparison of bulk PXRD and the calculated spectrum of the solution-grown crystals (Figure 3B). The nanobeam electron diffraction (NBED) patterns of these surface-bound MOFs consist of sharp spots, which match well with the

simulated diffraction patterns of the crystals grown in solution (Figure 3C and 3D).

Micro-Raman spectroscopy further confirmed that the crystals grown in solution and on surfaces have the same composition and structural features (Figure 3E). For example,

the ethylenic double bonds observed at $\nu = 1634.8 \text{ cm}^{-1}$ arise from the coordination between ligands and Ni(II). Changes of bands at $\nu = 1607.5$ (vs) and $\nu = 1634.8$ (s) cm^{-1} are indicative of the coordination between the pyridine moieties of **Ad-DB** with the metal centers.

The surface-bound MOFs can be detached by sonication, as demonstrated for the crystals obtained using NiBr_2 (Figures 4A and S17). This one-step on-surface crystallization and the subsequent detachment is another tool used to control the morphology of these uniform structures. To demonstrate the porosity and accessibility of the continuous channels of macroscopically oriented surface-bound MOFs, we immersed an ITO substrate covered with NiBr_2 -based crystals (30 min) and surface-detached crystals (24 h) in an ethanol solution of sodium resorufin (dimensions $5 \text{ \AA} \times 10 \text{ \AA}$) (Scheme 1, Figures 4A and S18). Confocal fluorescent microscopy revealed the presence of red crystals on the surface (Figure 1K), indicating that the dye molecules were successfully incorporated. Strong dichroism was observed under polarized light for the detached crystals (Figure 4B). When the polarization direction is parallel to the optical axis, the crystals are clearly purple. However, when the polarization direction is perpendicular to the optical axis, the crystals are almost colorless. These crystals also show polarized-dependent emission with the highest intensity when the excitation light is parallel to the optical axis of the crystal (Figure 4C). Excitation–emission measurements showed two main emission peaks of sodium resorufin at $\lambda = 610$ and 635 nm (Figure 4D). These optical properties demonstrate the supramolecular alignment of the dyes inside the 1D channels.

Crystals from **AD-DB** and NiBr_2 formed both in solution and on surfaces exhibit Kleinman-forbidden SHG responses as a result of the 622 symmetry (Figures 5 and S19). A signal is observed at $\lambda = 470 \text{ nm}$ when excited at $\lambda = 940 \text{ nm}$ with SHG microscopy. The frequency doubling is also observed when varying the excitation wavelength (Figure S20). In order to explore the local structural variations, we performed SHG measurements on individual crystals. The SHG signal intensity maps are polarization dependent. When the exciting polarization at $\lambda = 1000 \text{ nm}$ was perpendicular to the major crystal axis (Figure 5A), a strong signal appeared from the center of the crystal with the same polarization (Figure 5B and 5D). Exciting with polarization parallel to the crystal axis resulted in increased signals from the particle edges (Figure 5C and 5E). This polarization-dependent SHG is most likely due to the large size of the crystal together with the convex morphology causing refraction and scattering of the incident and emitted light.⁵⁵ The polar plot presents the SHG intensity along two polarization axes as a function of excitation polarization. To confirm the symmetry of the signals from both the center and the edges in the polar plot, we performed a numerical calculation. Assuming the existence of the point symmetry group 622 (but not taking into account the exact particle geometry), the calculated polarized SHG patterns are very close to the experimentally observed patterns (Figure 5F). The second-order nonlinearity $|d_{\text{eff}}|$ value was quantified using hyper-Rayleigh scattering (HRS) (Tables S2 and S3). ZnO crystals with a similar shape were used as a reference (Figure S21). This method can characterize the average hyperpolarizability $\langle \beta^2 \rangle$. On the basis of this extracted value, it is possible to infer the bulk equivalent value of the nonlinear susceptibility tensor $\chi^{(2)}$, which is manifested by a reduced representation d_{ijk} value. For a material with 622 symmetry,

there are only two components: $d_{14} = -d_{25}$. The $|d_{\text{eff}}|$ value was found to be 17.8 pm V^{-1} , which is ~ 13 times higher than urea ($d_{xyz} = 1.4 \text{ pm V}^{-1}$).⁶⁹ This value is very high for a Kleinmann-forbidden transition. Literature values are typically well below 1 pm/V , and even at very near-resonance conditions values have been reported of below 10 pm/V .⁸⁰ Chen et al. reported on strong Kleinman-forbidden SHG in a chiral sulfide ($\text{La}_4\text{InSbS}_9$).⁸¹ They roughly estimated a value of 20 pm/V , which is comparable to the value obtained here. Simulations suggest that the SHG originates from lattice vibrations. Our values of $\chi^{(2)}$ are relatively large even when comparing to MOFs with chiral ligands where SHG is not symmetry forbidden and are moderately high for MOFs in general.^{69,82}

CONCLUSIONS

The presented study can be considered as a new entry to the formation of individually surface-bound and oriented MOFs (sMOFs) on transparent and conductive substrates. The one-step approach allows modulator-free control over the shape and dimensions while maintaining a high level of monodispersity. Whereas the SURMOF chemistry can affect the packing,^{43,44} our surface-bound MOFs have a nearly identical packing as the solution-grown MOFs. A remarkable correlation between the growth, morphology, and uniformity of the solution and the surface-bound crystals was demonstrated. Similar mechanistic pathways for the formation of the morphologically different crystals might exist. The crystallographic packing exhibits chirality at different levels; it represents rare examples of crystals whose achiral molecular components are arranged in the $P622$ space group. The use of different coordinative counteranions (Br^- , Cl^- , NO_3^- , and OAc^-), metal cations (Ni^{2+} , Cu^{2+}), growth conditions, and similar ligands (having triple instead of double carbon–carbon bonds) results in nearly identical chiral framework structures.⁶⁶ These observations indicate that a new class of chiral crystals is achievable using metal cations known to form an octahedral molecular geometry with four pyridine moieties in plane. Although the crystallographic structures are nearly identical, the crystals can take on many sizes and forms, ranging from achiral mono- to chiral multidomain morphologies. The use of surface chemistry allows us to generate crystals representing only one-half of the structures formed in solution. The postcrystallization modification of the crystals with arrays of aligned dyes in the macroscopically oriented, continuous channels is an interesting feature. SHG-active MOFs have been designed by Lin and others^{69,82} and have been shown to have better properties in comparison to many materials grown by other methods. SHG-active surface-bound MOFs have been less explored. The dependence of both the absorption and the emission properties of the SHG-active crystals on the polarization of the applied light indicates that they are suitable candidates for the formation of optical switches.

ASSOCIATED CONTENT

Supporting Information

The Supporting Information is available free of charge at <https://pubs.acs.org/doi/10.1021/jacs.0c05384>.

Details about the characterization methods, experimental procedures, and data (PDF)

MOF-NiBr₂-M; CCDC: 1965784 (CIF)

MOF-Ni(OAc)₂-M; CCDC: 1965788 (CIF)
Ad-DB; CCDC: 1965785 (CIF)
MOF-Ni(OAc)₂-P; CCDC: 1992014 (CIF)
MOF-NiBr₂-P; CCDC: 1965786 (CIF)

AUTHOR INFORMATION

Corresponding Authors

Michal Lahav – Department of Organic Chemistry, Weizmann Institute of Science, Rehovot 7610001, Israel;
Email: michal.lahav@weizmann.ac.il
Milko E. van der Boom – Department of Organic Chemistry, Weizmann Institute of Science, Rehovot 7610001, Israel;
orcid.org/0000-0003-4102-4220;
Email: milko.vanderboom@weizmann.ac.il

Authors

Qiang Wen – Department of Organic Chemistry, Weizmann Institute of Science, Rehovot 7610001, Israel
Shira Tenenholtz – Department of Organic Chemistry, Weizmann Institute of Science, Rehovot 7610001, Israel
Linda J. W. Shimon – Department of Chemical Research Support, Weizmann Institute of Science, Rehovot 7610001, Israel; orcid.org/0000-0002-7861-9247
Omri Bar-Elli – Physics of Complex Systems, Weizmann Institute of Science, Rehovot 7610001, Israel
Lior M. Beck – Physics of Complex Systems, Weizmann Institute of Science, Rehovot 7610001, Israel
Lothar Houben – Department of Chemical Research Support, Weizmann Institute of Science, Rehovot 7610001, Israel
Sidney R. Cohen – Department of Chemical Research Support, Weizmann Institute of Science, Rehovot 7610001, Israel;
orcid.org/0000-0003-4255-3351
Yishay Feldman – Department of Chemical Research Support, Weizmann Institute of Science, Rehovot 7610001, Israel
Dan Oron – Physics of Complex Systems, Weizmann Institute of Science, Rehovot 7610001, Israel; orcid.org/0000-0003-1582-8532

Complete contact information is available at:
<https://pubs.acs.org/10.1021/jacs.0c05384>

Notes

The authors declare no competing financial interest.

ACKNOWLEDGMENTS

This research was supported by the Irving and Cherna Moskowitz Center for Nano and Bioimaging, the Israel Science Foundation (ISF), the Minerva Foundation, the Helen and Martin Kimmel Center for Molecular Design, and the Horizon 2020 Research and Innovation program of the European Union under the Marie Skłodowska-Curie grant agreement no. 642192. We thank Dr. I. Pinkas (Raman spectroscopy), Dr. V. Kalchenko (SHG imaging), Dr Y. Addadi (confocal fluorescent microscopy), and K. Rechav (FIB-SEM) for their advice and measurements. We thank ESRF and the ID29 beamline scientists for time and support. M.E.v.d.B. holds the Bruce A. Pearlman Professional Chair in Synthetic Organic Chemistry.

REFERENCES

(1) Yanai, N.; Granick, S. Directional self-assembly of a colloidal metal–organic framework. *Angew. Chem., Int. Ed.* **2012**, *51*, 5638–5641.

(2) Liang, H.; Yang, H.; Wang, W.; Li, J.; Xu, H. High-yield uniform synthesis and microstructure-determination of rice-shaped silver nanocrystals. *J. Am. Chem. Soc.* **2009**, *131*, 6068–6069.

(3) Pang, M.; Cairns, A. J.; Liu, Y.; Belmabkhout, Y.; Zeng, H. C.; Eddaoudi, M. Highly monodisperse M(III)-based soc-MOFs (M = In and Ga) with cubic and truncated cubic morphologies. *J. Am. Chem. Soc.* **2012**, *134*, 13176–13179.

(4) Hollingsworth, M. D. Crystal engineering: From structure to function. *Science* **2002**, *295*, 2410–2413.

(5) Desiraju, G. R. Crystal engineering: From molecule to crystal. *J. Am. Chem. Soc.* **2013**, *135*, 9952–9967.

(6) Ma, T.; Kapustin, E. A.; Yin, S. X.; Liang, L.; Zhou, Z.; Niu, J.; Li, L.-H.; Wang, Y.; Su, J.; Li, J.; Wang, X.; Wang, W. D.; Wang, W.; Sun, J.; Yaghi, O. M. Single-crystal X-ray diffraction structures of covalent organic frameworks. *Science* **2018**, *361*, 48–52.

(7) Aizenberg, J.; Black, A. J.; Whitesides, G. M. Control of crystal nucleation by patterned self-assembled monolayers. *Nature* **1999**, *398*, 495–498.

(8) Aizenberg, J.; Black, A. J.; Whitesides, G. M. Oriented growth of calcite controlled by self-assembled monolayers of functionalized alkanethiols supported on gold and silver. *J. Am. Chem. Soc.* **1999**, *121*, 4500–4509.

(9) Landau, E. M.; Levanon, M.; Leiserowitz, L.; Lahav, M.; Sagiv, J. Transfer of structural information from Langmuir monolayers to three-dimensional growing crystals. *Nature* **1985**, *318*, 353–356.

(10) Mastai, Y. Enantioselective crystallization on nano-chiral surfaces. *Chem. Soc. Rev.* **2009**, *38*, 772–780.

(11) Wang, X.; Simard, M.; Wuest, J. D. Molecular tectonics. Three-dimensional organic networks with zeolitic properties. *J. Am. Chem. Soc.* **1994**, *116*, 12119–12120.

(12) Kissel, P.; Murray, D. J.; Wulfstange, W. J.; Catalano, V. J.; King, B. T. A nanoporous two-dimensional polymer by single-crystal-to-single-crystal photopolymerization. *Nat. Chem.* **2014**, *6*, 774–778.

(13) Kory, M. J.; Wörle, M.; Weber, T.; Payamyar, P.; van de Poll, S. W.; Dshemuchadse, J.; Trapp, N.; Schlüter, A. D. Gram-scale synthesis of two-dimensional polymer crystals and their structure analysis by X-ray diffraction. *Nat. Chem.* **2014**, *6*, 779–784.

(14) Wang, H.; Li, B.; Wu, H.; Hu, T.-L.; Yao, Z.; Zhou, W.; Xiang, S.; Chen, B. A flexible microporous hydrogen-bonded organic framework for gas sorption and separation. *J. Am. Chem. Soc.* **2015**, *137*, 9963–9970.

(15) Sindoro, M.; Yanai, N.; Jee, A.-Y.; Granick, S. Colloidal-sized metal–organic frameworks: Synthesis and applications. *Acc. Chem. Res.* **2014**, *47*, 459–469.

(16) Cai, X.; Lin, J.; Pang, M. Facile synthesis of highly uniform Fe-MIL-88B particles. *Cryst. Growth Des.* **2016**, *16*, 3565–3568.

(17) Cho, W.; Lee, H. J.; Oh, M. Growth-controlled formation of porous coordination polymer particles. *J. Am. Chem. Soc.* **2008**, *130*, 16943–16946.

(18) Umemura, A.; Diring, S.; Furukawa, S.; Uehara, H.; Tsuruoka, T.; Kitagawa, S. Morphology design of porous coordination polymer crystals by coordination modulation. *J. Am. Chem. Soc.* **2011**, *133*, 15506–155013.

(19) Kitagawa, S.; Kitaura, R.; Noro, S. Functional porous coordination polymers. *Angew. Chem., Int. Ed.* **2004**, *43*, 2334–2375.

(20) Zhou, H.-C. J.; Kitagawa, S. Metal–organic frameworks (MOFs). *Chem. Soc. Rev.* **2014**, *43*, 5415–5418.

(21) Zhou, H.-C.; Long, J. R.; Yaghi, O. M. Introduction to metal–organic frameworks. *Chem. Rev.* **2012**, *112*, 673–674.

(22) Rosi, N. L.; Eckert, J.; Eddaoudi, M.; Vodak, D. T.; Kim, J.; Keefe, M.; Yaghi, O. M. Hydrogen storage in microporous metal–organic frameworks. *Science* **2003**, *300*, 1127–1129.

(23) Connolly, B. M.; Madden, D. G.; Wheatley, A. E. H.; Fairen-Jimenez, D. Shaping the future of fuel: Monolithic metal–organic frameworks for high-density gas storage. *J. Am. Chem. Soc.* **2020**, *142*, 8541–8549.

(24) Trickett, C. A.; Helal, A.; Al-Maythaly, B. A.; Yamani, Z. H.; Cordova, K. E.; Yaghi, O. M. The chemistry of metal–organic

frameworks for CO₂ capture, regeneration and conversion. *Nat. Rev. Mater.* **2017**, *2*, 17045.

(25) Han, X.; Yang, S.; Schröder, M. Porous metal–organic frameworks as emerging sorbents for clean air. *Nat. Rev. Chem.* **2019**, *3*, 108–118.

(26) Reed, D. A.; Keitz, B. K.; Oktawiec, J.; Mason, J. A.; Runčevski, T.; Xiao, D. J.; Darago, L. E.; Crocellà, V.; Bordiga, S.; Long, J. R. A spin transition mechanism for cooperative adsorption in metal–organic frameworks. *Nature* **2017**, *550*, 96–100.

(27) Chen, Z.; Li, P.; Anderson, R.; Wang, X.; Zhang, X.; Robison, L.; Redfern, L. R.; Moribe, S.; Islamoglu, T.; Gómez-Gualdrón, D. A.; Yildirim, T.; Stoddart, J. F.; Farha, O. K. Balancing volumetric and gravimetric uptake in highly porous materials for clean energy. *Science* **2020**, *368*, 297–303.

(28) Li, L.; Lin, R.-B.; Krishna, R.; Li, H.; Xiang, S.; Wu, H.; Li, J.; Zhou, W.; Chen, B. Ethane/ethylene separation in a metal–organic framework with iron-peroxo sites. *Science* **2018**, *362*, 443–446.

(29) Denny, M. S.; Moreton, J. C.; Benz, L.; Cohen, S. M. Metal–organic frameworks for membrane-based separations. *Nat. Rev. Mater.* **2016**, *1*, 16078.

(30) Krause, S.; Bon, V.; Senkowska, I.; Stoeck, U.; Wallacher, D.; Többsens, D. M.; Zander, S.; Pillai, R. S.; Maurin, G.; Coudert, F.-X.; Kaskel, S. A pressure-amplifying framework material with negative gas adsorption transitions. *Nature* **2016**, *532*, 348–352.

(31) Nugent, P.; Belmabkhout, Y.; Burd, S. D.; Cairns, A. J.; Luebke, R.; Forrest, K.; Pham, T.; Ma, S.; Space, B.; Wojtas, L.; Eddaoudi, M.; Zaworotko, M. J. Porous materials with optimal adsorption thermodynamics and kinetics for CO₂ separation. *Nature* **2013**, *495*, 80–84.

(32) Strauss, I.; Mundstock, A.; Treger, M.; Lange, K.; Hwang, S.; Chmelik, C.; Rusch, P.; Bigall, N. C.; Pichler, T.; Shiozawa, H.; Caro, J. Metal–organic framework Co-MOF-74-based host–guest composites for resistive gas sensing. *ACS Appl. Mater. Interfaces* **2019**, *11*, 14175–14181.

(33) Neumann, C. N.; Rozeveld, S. J.; Yu, M.; Rieth, A. J.; Dincă, M. Metal–organic framework-derived guerdet catalyst effectively differentiates between ethanol and butanol. *J. Am. Chem. Soc.* **2019**, *141*, 17477–17481.

(34) Baek, J.; Rungtaweivoranit, B.; Pei, X.; Park, M.; Fakra, S. C.; Liu, Y.-S.; Matheu, R.; Alshimiri, S. A.; Alshehri, S.; Trickett, C. A.; Somorjai, G. A.; Yaghi, O. M. Bioinspired metal–organic framework catalysts for selective methane oxidation to methanol. *J. Am. Chem. Soc.* **2018**, *140*, 18208–18216.

(35) Drake, T.; Ji, P.; Lin, W. Site isolation in metal–organic frameworks enables novel transition metal catalysis. *Acc. Chem. Res.* **2018**, *51*, 2129–2138.

(36) Gu, Z.-G.; Zhan, C.; Zhang, J.; Bu, X. Chiral chemistry of metal–camphorate frameworks. *Chem. Soc. Rev.* **2016**, *45*, 3122–3144.

(37) Tan, C.; Yang, K.; Dong, J.; Liu, Y.; Liu, Y.; Jiang, J.; Cui, Y. Boosting enantioselectivity of chiral organocatalysts with ultrathin two-dimensional metal–organic framework nanosheets. *J. Am. Chem. Soc.* **2019**, *141*, 17685–17695.

(38) Wanderley, M. M.; Wang, C.; Wu, C.-D.; Lin, W. A chiral porous metal–organic framework for highly sensitive and enantioselective fluorescence sensing of amino alcohols. *J. Am. Chem. Soc.* **2012**, *134*, 9050–9053.

(39) Corella-Ochoa, M. N.; Tapia, J. B.; Rubin, H. N.; Lillo, V.; González-Cobos, J.; Núñez-Rico, J. L.; Balestra, S. R. G.; Almora-Barrios, N.; Lledós, M.; Güell-Bara, A.; Cabezas-Giménez, J.; Escudero-Adán, E. C.; Vidal-Ferran, A.; Calero, S.; Reynolds, M.; Martí-Gastaldo, C.; Galán-Mascarós, J. R. Homochiral metal–organic frameworks for enantioselective separations in liquid chromatography. *J. Am. Chem. Soc.* **2019**, *141*, 14306–14316.

(40) Van Vleet, M. J.; Weng, T.; Li, X.; Schmidt, J. R. In situ, time-resolved, and mechanistic studies of metal–organic framework nucleation and growth. *Chem. Rev.* **2018**, *118*, 3681–3721.

(41) Schoedel, A.; Li, M.; Li, D.; O’Keeffe, M.; Yaghi, O. M. Structures of metal–organic frameworks with rod secondary building units. *Chem. Rev.* **2016**, *116*, 12466–12535.

(42) Noro, S.; Kitaura, R.; Kondo, M.; Kitagawa, S.; Ishii, T.; Matsuzaka, H.; Yamashita, M. Framework engineering by anions and porous functionalities of Cu(II)/4,4’-bpy coordination polymers. *J. Am. Chem. Soc.* **2002**, *124*, 2568–2583.

(43) Shekhah, O.; Liu, J.; Fischer, R. A.; Wöll, C. MOF thin films: Existing and future applications. *Chem. Soc. Rev.* **2011**, *40*, 1081–1106.

(44) Shekhah, O.; Wang, H.; Paradinas, M.; Ocal, C.; Schüpbach, B.; Terfort, A.; Zacher, D.; Fischer, R. A.; Wöll, C. Controlling interpenetration in metal–organic frameworks by liquid-phase epitaxy. *Nat. Mater.* **2009**, *8*, 481–484.

(45) Chernikova, V.; Shekhah, O.; Eddaoudi, M. Advanced fabrication method for the preparation of MOF thin films: Liquid-phase epitaxy approach meets spin coating method. *ACS Appl. Mater. Interfaces* **2016**, *8*, 20459–20464.

(46) Goswami, S.; Hod, I.; Duan, J. D.; Kung, C.-W.; Rimoldi, M.; Malliakas, C. D.; Palmer, R. H.; Farha, O. K.; Hupp, J. T. Anisotropic redox conductivity within a metal–organic framework material. *J. Am. Chem. Soc.* **2019**, *141*, 17696–17702.

(47) Falcaro, P.; Ricco, R.; Doherty, C. M.; Liang, K.; Hill, A. J.; Styles, M. J. MOF positioning technology and device fabrication. *Chem. Soc. Rev.* **2014**, *43*, 5513–5560.

(48) Schoedel, A.; Scherb, C.; Bein, T. Oriented nanoscale films of metal–organic frameworks by room-temperature gel-layer synthesis. *Angew. Chem., Int. Ed.* **2010**, *49*, 7225–7228.

(49) Shen, D.; Wang, G.; Liu, Z.; Li, P.; Cai, K.; Cheng, C.; Shi, Y.; Han, J.-M.; Kung, C.-W.; Gong, X.; Guo, Q.-H.; Chen, H.; Sue, A. C. H.; Botros, Y. Y.; Facchetti, A.; Farha, O. K.; Marks, T. J.; Stoddart, J. F. Epitaxial growth of γ -cyclodextrin-containing metal–organic frameworks based on a host–guest strategy. *J. Am. Chem. Soc.* **2018**, *140*, 11402–11407.

(50) Falcaro, P.; Okada, K.; Hara, T.; Ikigaki, K.; Tokudome, Y.; Thornton, A. W.; Hill, A. J.; Williams, T.; Doonan, C.; Takahashi, M. Centimetre-scale micropore alignment in oriented polycrystalline metal–organic framework films via heteroepitaxial growth. *Nat. Mater.* **2017**, *16*, 342–348.

(51) Gu, Z.-G.; Zhang, J. Epitaxial growth and applications of oriented metal–organic framework thin films. *Coord. Chem. Rev.* **2019**, *378*, 513–532.

(52) Luo, J.; Li, Y.; Zhang, H.; Wang, A.; Lo, W.-S.; Dong, Q.; Wong, N.; Povinelli, C.; Shao, Y.; Chereddy, S.; Wunder, S.; Mohanty, U.; Tsung, C.-K.; Wang, D. A metal–organic framework thin film for selective Mg²⁺ transport. *Angew. Chem., Int. Ed.* **2019**, *58*, 15313–15317.

(53) Wannapaiboon, S.; Schneemann, A.; Hante, I.; Tu, M.; Epp, K.; Semrau, A. L.; Sternemann, C.; Paulus, M.; Baxter, S. J.; Kieslich, G.; Fischer, R. A. Control of structural flexibility of layered-pillared metal–organic frameworks anchored at surfaces. *Nat. Commun.* **2019**, *10*, 346.

(54) Yu, X.-J.; Xian, Y.-M.; Wang, C.; Mao, H.-L.; Kind, M.; Abu-Husein, T.; Chen, Z.; Zhu, S.-B.; Ren, B.; Terfort, A.; Zhuang, J.-L. Liquid-phase epitaxial growth of highly oriented and multivariate surface-attached metal–organic frameworks. *J. Am. Chem. Soc.* **2019**, *141*, 18984–18993.

(55) Venkatakrishnarao, D.; Narayana, Y. S. L. V.; Mohaidon, M. A.; Mamonov, E. A.; Mitetelo, N.; Kolmychek, I. A.; Maydykovskiy, A. I.; Novikov, V. B.; Murzina, T. V.; Chandrasekar, R. Two-photon luminescence and second-harmonic generation in organic nonlinear surface comprised of self-assembled frustum shaped organic micro-lasers. *Adv. Mater.* **2017**, *29*, 1605260.

(56) Cho, J.; Ishida, Y. Macroscopically oriented porous materials with periodic ordered structures: From zeolites and metal–organic frameworks to liquid-crystal-templated mesoporous materials. *Adv. Mater.* **2017**, *29*, 1605974.

- (57) Feng, S.; Bein, T. Vertical aluminophosphate molecular sieve crystals grown at inorganic-organic interfaces. *Science* **1994**, *265*, 1839–1841.
- (58) Jiang, S.; Song, Q.; Massey, A.; Chong, S. Y.; Chen, L.; Sun, S.; Hasell, T.; Raval, R.; Sivaniah, E.; Cheetham, A. K.; Cooper, A. I. Oriented two-dimensional porous organic cage crystals. *Angew. Chem., Int. Ed.* **2017**, *56*, 9391–9395.
- (59) Cook, T. R.; Zheng, Y.-R.; Stang, P. J. Metal–organic frameworks and self-assembled supramolecular coordination complexes: Comparing and contrasting the design, synthesis, and functionality of metal–organic materials. *Chem. Rev.* **2013**, *113*, 734–777.
- (60) Inokuma, Y.; Arai, T.; Fujita, M. Networked molecular cages as crystalline sponges for fullerenes and other guests. *Nat. Chem.* **2010**, *2*, 780–783.
- (61) Rizzuto, F. J.; Nitschke, J. R. Narcissistic, integrative, and kinetic self-sorting within a system of coordination cages. *J. Am. Chem. Soc.* **2020**, *142*, 7749–7753.
- (62) Wang, H.; Li, Y.; Yu, H.; Song, B.; Lu, S.; Hao, X.-Q.; Zhang, Y.; Wang, M.; Hla, S.-W.; Li, X. Combining synthesis and self-assembly in one pot to construct complex 2d metallo-supramolecules using terpyridine and pyrylium salts. *J. Am. Chem. Soc.* **2019**, *141*, 13187–13195.
- (63) Guo, Q.-H.; Liu, Z.; Li, P.; Shen, D.; Xu, Y.; Ryder, M. R.; Chen, H.; Stern, C. L.; Malliakas, C. D.; Zhang, X.; Zhang, L.; Qiu, Y.; Shi, Y.; Snurr, R. Q.; Philp, D.; Farha, O. K.; Stoddart, J. F. A hierarchical nanoporous diamondoid superstructure. *Chem.* **2019**, *5*, 2353–2364.
- (64) Rajput, A.; Mukherjee, R. Coordination chemistry with pyridine/pyrazine amide ligands. Some noteworthy results. *Coord. Chem. Rev.* **2013**, *257*, 350–368.
- (65) Shankar, S.; Balgley, R.; Lahav, M.; Cohen, S. R.; Popovitz-Biro, R.; van der Boom, M. E. Metal–organic microstructures: From rectangular to stellated and interpenetrating polyhedra. *J. Am. Chem. Soc.* **2015**, *137*, 226–231.
- (66) di Gregorio, M. C.; Shimon, L. J. W.; Brumfeld, V.; Houben, L.; Lahav, M.; van der Boom, M. E. Emergence of chirality and structural complexity in single crystals at the molecular and morphological levels. *Nat. Commun.* **2020**, *11*, 380.
- (67) di Gregorio, M. C.; Ranjan, P.; Houben, L.; Shimon, L. J. W.; Rechav, K.; Lahav, M.; van der Boom, M. E. Metal-coordination-induced fusion creates hollow crystalline molecular superstructures. *J. Am. Chem. Soc.* **2018**, *140*, 9132–9139.
- (68) Shankar, S.; Chovnik, O.; Shimon, L. J. W.; Lahav, M.; van der Boom, M. E. Directed molecular structure variations of three-dimensional halogen-bonded organic frameworks (XBOFs). *Cryst. Growth Des.* **2018**, *18*, 1967–1977.
- (69) Wang, C.; Zhang, T.; Lin, W. Rational synthesis of noncentrosymmetric metal–organic frameworks for second-order nonlinear optics. *Chem. Rev.* **2012**, *112*, 1084–1104.
- (70) Flack, H. D.; Bernardinelli, G. The use of X-ray crystallography to determine absolute configuration. *Chirality* **2008**, *20*, 681–690.
- (71) Rosenthal, M. R.; Drago, R. S. Pyridine complexes of nickel(II). *Inorg. Chem.* **1965**, *4*, 840–844.
- (72) Neumann, T.; Jess, I.; Näther, C. Crystal structures of (acetonitrile- κN)tris(pyridine-4-thioamide- κN)bis(thiocyanato- κN)-cobalt(II) acetonitrile disolvate and tetrakis(pyridine-4-thioamide- κN)bis(thiocyanato- κN)nickel(II) methanol pentasolvate. *Acta Crystallogr. E* **2018**, *74*, 964–969.
- (73) Hamm, D. J.; Bordner, J.; Schreiner, A. F. The crystal and molecular structure of diiodotetrakis(pyridine)nickel(II) [Nipy₄I₂]. *Inorg. Chim. Acta* **1973**, *7*, 637–641.
- (74) Wöhlert, S.; Wriedt, M.; Jess, I.; Näther, C. Bis(dicyanamido- κN)tetrakis(pyridine- κN)nickel(II). *Acta Crystallogr., Sect. E: Struct. Rep. Online* **2012**, *68*, E68–m745.
- (75) Bachman, R. E.; Whitmire, K. H.; Mandal, S.; Bharadwaj, P. K. Dichlorotetra-kis(pyridine)nickel(II). *Acta Crystallogr., Sect. C: Cryst. Struct. Commun.* **1992**, *48*, 1836–1837.
- (76) Dryzun, C.; Mastai, Y.; Shvalb, A.; Avnir, D. Chiral silicate zeolites. *J. Mater. Chem.* **2009**, *19*, 2062–2069.
- (77) Blatov, V. A.; Shevchenko, A. P.; Proserpio, D. M. Applied topological analysis of crystal structures with the program package ToposPro. *Cryst. Growth Des.* **2014**, *14*, 3576–3586.
- (78) On-surface crystal growth from Ad-DB and NiCl₂ was not explored because of the small sizes obtained for the crystals grown in solution.
- (79) Roberts, R. J.; Rowe, R. C.; York, P. The relationship between young's modulus of elasticity of organic solids and their molecular structure. *Powder Technol.* **1991**, *65*, 139–146.
- (80) In *Metal-Organic Frameworks for Photonic Applications*; Chen, B., Qian, G., Eds.; Springer: London, 2014.
- (81) Zhao, H.-J.; Zhang, Y.-F.; Chen, L. Strong Kleinman-forbidden second harmonic generation in chiral sulfide: La₄InSbS₉. *J. Am. Chem. Soc.* **2012**, *134*, 1993–1995.
- (82) Mingabudinova, L. R.; Vinogradov, V. V.; Milichko, V. A.; Hey-Hawkins, E.; Vinogradov, A. V. Metal–organic frameworks as competitive materials for non-linear optics. *Chem. Soc. Rev.* **2016**, *45*, 5408–5431.